Title

Time-Dependent Physicochemical Changes of Carbonate Surfaces from SmartWater (Diluted Seawater) Flooding Processes for Improved Oil Recovery

Journal

Langmuir, 35(1)

ISSN

0743-7463

Authors

Chen, Szu-Ying
Kristiansen, Kai
Seo, Dongjin
et al.

Publication Date

2019-01-08

DOI

10.1021/acs.langmuir.8b02711

Peer reviewed

LANGMUIR
Cite This: *Langmuir* 2019, 35, 41−50
Article
pubs.acs.org/Langmuir

Time-Dependent Physicochemical Changes of Carbonate Surfaces from SmartWater (Diluted Seawater) Flooding Processes for Improved Oil Recovery

Szu-Ying Chen,[*,†] Kai Kristiansen,[†] Dongjin Seo,[†,⊥] Nicholas A. Cadirov,[†] Howard A. Dobbs,[†] Yair Kaufman,[†,#] Alex M. Schrader,[†] Roberto C. Andresen Eguiluz,[†] Mohammed B. Alotaibi,[‡] Subhash C. Ayirala,[‡] James R. Boles,[§] Ali A. Yousef,[‡] and Jacob N. Israelachvili[†,∥]

[†]Department of Chemical Engineering, [§]Department of Earth Science, and [∥]Materials Department, University of California, Santa Barbara, California 93106, United States

[‡]The Exploration and Petroleum Engineering Center - Advanced Research Center (EXPEC ARC), Saudi Aramco, Dhahran 34465, Saudi Arabia

Supporting Information

ABSTRACT: Over the past few decades, field- and laboratory-scale studies have shown enhancements in oil recovery when reservoirs, which contain high-salinity formation water (FW), are waterflooded with modified-salinity salt water (widely referred to as the low-salinity, dilution, or SmartWater effect for improved oil recovery). In this study, we investigated the time dependence of the physicochemical processes that occur during diluted seawater (i.e., SmartWater) waterflooding processes of specific relevance to carbonate oil reservoirs. We measured the changes to oil/water/rock wettability, surface roughness, and surface chemical composition during SmartWater flooding using 10-fold-diluted seawater under mimicked oil reservoir conditions with calcite and carbonate reservoir rocks. Distinct effects due to SmartWater flooding were observed and found to occur on two different timescales: (1) a rapid (<15 min) increase in the colloidal electrostatic double-layer repulsion between the rock and oil across the SmartWater, leading to a decreased oil/water/rock adhesion energy and thus increased water wetness and (2) slower (>12 h to complete) physicochemical changes of the calcite and carbonate reservoir rock surfaces, including surface roughening via the dissolution of rock and the reprecipitation of dissolved carbonate species after exchanging key ions (Ca^{2+}, Mg^{2+}, CO_3^{2-}, and SO_4^{2-} in carbonates) with those in the flooding SmartWater. Our experiments using crude oil from a carbonate reservoir reveal that these reservoir rock surfaces are covered with organic−ionic preadsorbed films (ad-layers), which the SmartWater removes (detaches) as flakes. Removal of the organic−ionic ad-layers by SmartWater flooding enhances oil release from the surfaces, which was found to be critical to increasing the water wetness and significantly improving oil removal from carbonates. Additionally, the increase in water wetness is further enhanced by roughening of the rock surfaces, which decreases the effective contact (interaction) area between the oil and rock interfaces. Furthermore, we found that the rate of these slower physicochemical changes to the carbonate rock surfaces increases with increasing temperature (at least up to an experimental temperature of 75 °C). Our results suggest that the effectiveness of improved oil recovery from SmartWater flooding depends strongly on the formation of the organic−ionic ad-layers. In oil reservoirs where the ad-layer is fully developed and robust, injecting SmartWater would lead to significant removal of the ad-layer and improved oil recovery.

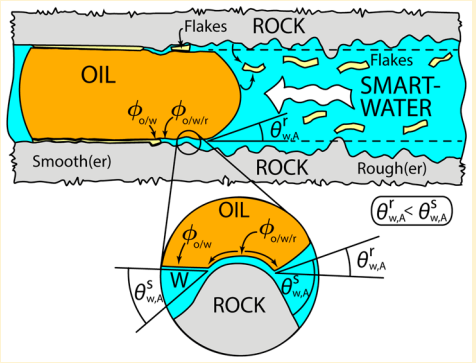

1. INTRODUCTION

Over the past few decades, waterflooding oil reservoirs with salt water of specific salinity (typically, low) and ionic composition, i.e., SmartWater, to increase oil recovery in both sandstone[1−4] and carbonate reservoirs[5−9] has become a promising alternative to other existing improved/enhanced oil recovery (IOR/EOR) techniques.[10−14] The underlying mechanisms of this relatively new IOR technique referred to as SmartWater flooding are poorly understood, especially in carbonate systems.[15] In sandstone reservoirs, the introduction of SmartWater composed of low-salinity brine water causes the migration of fines and changes in pH and wettability.[16−19] The presence of certain clays is essential for this SmartWater (or low-salinity) effect to occur in sandstones.[20] However, because clay coatings are not normally found in carbonate reservoirs, other mechanisms must be responsible for the improvement in oil recovery by using SmartWater, such as diluted seawater, in such reservoirs.

Received: August 9, 2018
Revised: December 1, 2018
Published: December 3, 2018

DOI: 10.1021/acs.langmuir.8b02711
Langmuir 2019, 35, 41−50

One widely accepted explanation for the SmartWater effect in carbonate reservoirs, which is also observed for sandstone reservoirs, is that SmartWater changes the oil/water/rock wettability to be more water-wet by increasing the electrostatic repulsion and thereby decreasing the adhesion energy, $W_{o/w/r}$, between the oil (o) and rock (r) surfaces across the salt water (w).[15,21] Investigating the SmartWater effect by varying the concentration of the SmartWater using high-salinity formation water (350 000 ppm), seawater (SW; 60 000 ppm), different dilutions of SW, and pure water, Chen et al.[21] found two additional chemically induced effects of SmartWater which occur on the nano- to millimeter length scales. First, in agreement with other reports, reducing the concentration of certain ionic species, e.g., carbonate, CO_3^{2-}, while concentrating others, e.g., sulfate, SO_4^{2-}, produces significant dissolution and reprecipitation of the rock surfaces, resulting in overall roughening.[21−26] Studies investigating these chemical effects have emphasized the importance of sulfate ions in the SmartWater for IOR in carbonate rocks.[10−12] These chemically induced morphological changes to the rock surface can dramatically enhance the water wetness,[27−30] giving rise to the SmartWater effect for IOR.

Second, Chen et al.[21] discovered the detachment of organic−ionic films from the rock surfaces arising from introducing SmartWater. Prior to introducing SmartWater, these films, composed of organic and ionic components, were found to be preabsorbed as ad-layers on the native rock surfaces that have been restored with their reservoir wettability (by equilibrating the rock surfaces with oil and high-salinity water at elevated temperatures and prolonged times.) (For more details, see ref 21.) After introducing the SmartWater, thin (∼100 nm) but long (∼1 mm) "flakes" were observed suspended in the SmartWater. The number density of the flakes detached from the rock surface (1 cm^2 rock sample size) increased with decreasing salinity of the SmartWater (e.g., 100-fold-diluted SW produced substantially more flakes than SW and 2-fold-diluted SW). Characterization of the flakes using SEM-EDS, XPS, and FTIR spectroscopy indicated that the detached ad-layer (flakes) is largely composed of organic compounds mixed with salts (predominately of Na, Cl, and Mg), derived from the formation water and diluted seawater, with little Ca content (i.e., the ad-layer is not derived from calcite, the underlying rock material). Chen et al.[21] proposed that it is this detachment of the organic−ionic ad-layers from the rock surfaces that directly removes oil from the surface that is subsequently transported and recovered. Additionally, the removal of these ad-layers also changes the rock surface chemistry by exposing the underlying water-wet (calcite) rock surface, thereby directly increasing the water wetness of the rock surface.

This article reports the temporal changes that occur on the rock surfaces due to the physicochemical processes that are responsible for the SmartWater flooding IOR in carbonate rocks. We used a variety of complementary techniques that probe the surface topography and chemistry and also carried out comprehensive measurements of dynamic contact angles (both advancing and receding) that reflect the wettability of the surfaces both transiently (nonequilibrium) and at thermodynamic equilibrium. We characterized the timescales of the wettability changes and related them to the corresponding time-dependent physicochemical changes at the rock surfaces, including changes to the physical colloidal interaction forces, surface chemistry, and roughness. We also highlight the, often unappreciated, effect of surface roughening on enhancing water wetness. Finally, we extended our work on model calcite surfaces to experiments using actual carbonate reservoir rock samples.

2. MATERIALS AND METHODS

2.1. Sample Preparation. *2.1.1. Materials.* The mineral samples were either epi-polished single-crystalline calcite (z axis vertical, 1.67 nm RMS roughness, 10 mm × 10 mm × 0.5 mm, MTI Corporation), synthesized calcite ($CaCO_3$) prepared in-house from solution (see Supporting Information (SI), Section S2.1.1 for the preparation procedure), or rock samples obtained from a carbonate oil reservoir (referred to as reservoir carbonate samples). Prior to use in the experiments, the reservoir carbonate samples were thoroughly cleaned with toluene (hereafter referred to as an oil-free sample) to remove organic compounds. The composition of the reservoir carbonate samples was verified as a combination of calcite and dolomite by XRD (Figure S1) and SEM-EDS (Figure S7A). To better observe the topographical changes, the reservoir carbonate samples were polished to prepare smooth surfaces for the SEM-EDS (Section 2.4) imaging and characterization experiments. The polished surfaces were each marked with scratches to easily locate the same area for imaging.

The crude oil (CO) sample was obtained from the same carbonate reservoir as for the rock sample. The oil is light with 34.1° API (American Petroleum Institute) gravity at 60 °F and 0.87 g/cm^3 density and 14.6 cP viscosity under ambient conditions. In addition, the SARA (saturates, aromatics, resins, and asphaltenes) composition and total acid number of the crude oil are shown in Table 1. Dead (i.e., degassed) crude oil was used in the experiments.

Table 1. Properties of the Crude Oil

components %	saturates	39.2
	aromatics	48.3
	resins	7.0
	asphaltenes	5.5
total acid number (mg of KOH/g of oil)		0.25

The experimental salt water solutions were prepared in-house using deionized water (18.2 MΩ·cm resistivity, Milli-Q) and reagent-grade chemicals (sodium chloride, calcium chloride, magnesium chloride, sodium sulfate, and sodium bicarbonate) obtained from Sigma-Aldrich. The salt water compositions for formation water (FW) and injected seawater (SW) were based on chemical analyses of water samples from the same carbonate reservoir (Table 2) to mimic those used in oil-field waterflooding. The SmartWater (a term that has been defined in the IOR field of the petroleum industry as any injection water of specific salinity and ionic composition customized for improved oil recovery)[31−33] studied in this work was 10-fold-diluted SW (abbreviated as 10× diluted SW), hereafter simply referred to as SmartWater. Ten-fold-diluted SW SmartWater was prepared by mixing SW with the appropriate amount of deionized water. All salt

Table 2. Chemical Analyses of Formation Water and Injected Seawater

ions	formation water (FW) (ppm)	injected seawater (SW) (ppm)
sodium	59 500	18 300
calcium	19 000	650
magnesium	2400	2100
sulfate	350	4300
chloride	132 100	32 200
bicarbonate	350	120
total dissolved solids (TDS)	213 700	57 700

DOI: 10.1021/acs.langmuir.8b02711
Langmuir 2019, 35, 41−50

water solutions were filtered using 0.2 μm polypropylene-based syringe filters (Anotop 10 IC) prior to use in experiments.

The saturation indices (SI) for the different calcium-containing minerals in FW, SW, and SmartWater are presented in Table 3. The values reported were calculated using the PHREEQC aqueous modeling software, assuming a constant pH 6 solution at atmospheric pressure and 75 °C referenced against the oxygen redox standard. Positive, zero, and negative SI values indicate supersaturation, equilibrium, and undersaturation, respectively.

Table 3. Saturation Indices (SI) for the Different Calcium-Containing Minerals

	calcite	aragonite	dolomite	anhydrite	gypsum
formation water (FW)	0.95	0.84	1.73	0.06	−0.27
injected seawater (SW)	−0.75	−0.87	−0.53	−0.29	−0.51
SmartWater (10× diluted SW)	−2.33	−2.44	−3.73	−1.46	−1.65

2.1.2. Mineral Surface Conditioning (Aging) Procedure. To mimic oil reservoir conditions (see SI Section S2.1.2 for more details), the clean, oil-free mineral samples were first immersed in formation water that was saturated with oil surfactants (abbreviated as FW-CO) at 75 or 100 °C for 24 h. FW-CO was prepared by equilibrating FW with CO (3 FW:1 CO by volume) in a sealed Teflon bottle at 100 °C for 24 h and then extracting the FW portion, which has become saturated with surfactants from the CO. Throughout this article, this stage is referred to as the aging stage. Aging the mineral samples restores the oil and ionic species to the surfaces, which thereby allows for subsequently studying the oil-rock/brine water interactions and changes in the next stage (described below).

To study the effect of changing the solution condition from FW-CO to SmartWater (10× diluted SW), the fully aged mineral samples were subsequently immersed in SmartWater at 75 or 100 °C for specified amounts of time, t_{SW}. Throughout this article, this second stage is referred to as the SmartWater flooding stage, which is synonymous with the dilution step in ref 21.

2.2. Dynamic Contact Angle Measurements. To simulate and study the dynamics of the changes in the wettability of the oil/water/rock system during SmartWater flooding, dynamic macroscopic contact angles of oil on the rock surface immersed in the brine water were measured using a video-based optical contact angle measuring system (DataPhysics OCA 15Pro). Fully aged calcite samples were immersed in ∼20 mL of SmartWater (10× diluted SW) in sealed glass vials at 100 °C for different amounts of SmartWater flooding time, t_{SW}, and dynamic contact angles were measured after each t_{SW} at room temperature and atmospheric pressure. (Previous studies have shown no discernible difference when measuring contact angles at temperatures in the range of 25 to 75 °C for the studied oil/water/rock system.[21]) The dynamic contact angle experiments were performed at a constant volumetric flow rate of 0.05 μL/s, which corresponded to a measured contact-line velocity of ∼3 μm/s, which is equivalent to ∼1 ft/day (the typical reservoir flooding/oil extraction rate[34]). The total volume of the oil droplet deposited onto the rock surface for each experiment was ∼5−7 μL. The oil droplet contacting the rock sample immersed in SmartWater was modeled as a truncated sphere. The reported water-side contact angles, θ_w, were the angles between the tangent (at the oil/water/rock contact line) to the truncated sphere and the horizontal base of the sphere (Figure 1). (Note: All of the contact angles reported in this article are contact angles on the water (aqueous) side, θ_w, adopting the convention used in the petroleum industry; see Figure 1.)

The $W_{o/w/r}$ adhesion energy and contact angle θ_w are related by the Young−Dupré equation

$$W_{o/w/r} = \gamma_{o/w}(1 - \cos\theta_w) \quad (1)$$

where $\gamma_{o/w}$ is the oil/water interfacial tension. Lower values of θ_w (higher water wetness) correspond to lower $W_{o/w/r}$ and imply higher oil recovery for systems that are at least partially oil-wet.

To fully characterize the oil/water/rock wettability after each amount of SmartWater flooding time, t_{SW}, three different types of contact angles were measured and compared (Figure 1): (A) water-receding, $\theta_{w,R}$, where oil was continuously injected onto the rock surface; (B) static after water-receding, $\theta_{w,RS}$, where oil injection stopped and the injection needle was detached from the deposited oil droplet (i.e., the volume of the deposited oil droplet remained constant); and (C) water-advancing, $\theta_{w,A}$, where oil was continuously withdrawn from the droplet.

2.3. Surface Forces Apparatus. The absolute combined changes in the thickness and roughness of the calcite surfaces over time due to dissolution, desorption, (re)precipitation, and roughening were imaged and monitored in situ and in real time during the SmartWater flooding process using a Surface Forces Apparatus (SurForce LLC SFA Mark III). Figure S2 shows a schematic of the SFA system and illustrates the use of the fringes of equal chromatic order (FECO) optical interferometry technique.[35] The SFA technique probes an area of ∼0.1 mm^2 and has subnanometer depth/height resolution in the absolute surface separation distance between two surfaces (perpendicular to the surface plane) and micrometer lateral resolution.

Polycrystalline synthesized calcite films with 10 nm RMS height roughness and crystal domains of ∼10 μm in lateral dimension were precipitated onto mica surfaces. The initial combined thickness of the two films for different experiments varied between 40 and 700 nm due to the complexity of the deposition.

In situ SFA measurements were obtained during the aging period as well as during the SmartWater flooding period. For the aging period (∼24 h at 75 ± 5 °C), a ∼100 μL droplet of FW-CO was injected between the two apposing calcite films. This restored the oil and ionic species on the calcite surfaces. Subsequently, the FW-CO was exchanged by flushing with ∼5 mL of SmartWater (10× diluted

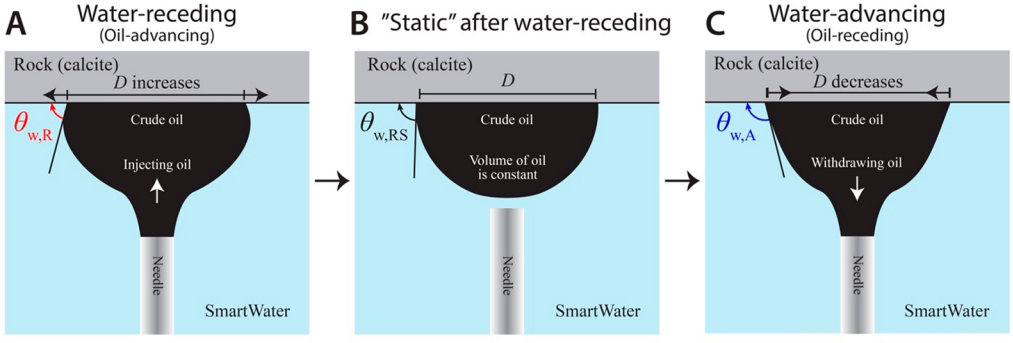

Figure 1. Schematic of the three types of measured contact angles of oil on rock in SmartWater: (A) water-receding, $\theta_{w,R}$; (B) static after water-receding, $\theta_{w,RS}$; and (C) water-advancing, $\theta_{w,A}$.

DOI: 10.1021/acs.langmuir.8b02711
Langmuir 2019, 35, 41−50

SW) to study the oil-rock/SmartWater/oil-rock interactions and topographical changes. The surfaces were separated by hundreds of micrometers when injecting the first solution (i.e., FW-CO) and when exchanging the solutions. To minimize the evaporation of the brine water droplet between the calcite surfaces, the SFA chamber was saturated with water vapor by adding a large reservoir of deionized water. In addition, the droplet size was monitored throughout the experiment and replenished with deionized water as needed to keep the droplet volume and concentration constant.

For each measurement, FECO images were captured after the calcite surfaces were compressed together to a few atmospheres in pressure. The procedure for finding the minimum and maximum combined calcite thicknesses is described in Figure S3. Between each measurement, the surfaces were separated by a few micrometers to avoid any dissolution caused by electrochemical reactions that may occur when two dissimilar surfaces (i.e., different crystallographic orientation, composition, or surface potential) are in close proximity.[36]

2.4. Scanning Electron Microscopy and Energy-Dispersive X-ray Spectroscopy. Scanning electron microscopy (SEM) images and energy-dispersive X-ray spectroscopy (EDS) spectra were acquired with an FEI XL30 Sirion FEG SEM with EBSD and EDX on the same reservoir carbonate samples described in Section 2.1.2, namely, the oil-free, fully aged, and after SmartWater flooding samples. The images were recorded with an electron beam voltage of 3−5 kV (to avoid damaging the rock surface) and magnifications ranging from 30× to 10 000×. In some instances, the sample was coated with a 70:30 Au/Pd thin film to improve the conductivity and image resolution, as indicated for the applicable images.

3. EXPERIMENTAL RESULTS

3.1. Oil/Water/Rock Wettability Changes Due to Smart-Water Flooding, Quantified via Dynamic Contact Angle Measurements. Changes to the wettability of the oil/water/rock system due to SmartWater flooding was quantified by measuring dynamic contact angles as a function of varying SmartWater flooding times, t_{SW} (defined in Section 2.1.2). An oil-wet or hydrophobic/oleophilic system is characterized by having a relatively high contact angle (on the water side), θ_w. The corresponding oil/water/rock adhesion energy, $W_{o/w/r}$ (related to θ_w by eq 1), is high and, by implication, the oil removal/recovery is low. On the other hand, a water-wet or hydrophilic/oleophobic system is characterized by having relatively low θ_w and low $W_{o/w/r}$, implying high oil removal/recovery.

The geometry of the droplet for measuring the static after water-receding contact angle (hereafter interchangeably referred to as the static contact angle), $\theta_{w,RS}$ (Figure 1B), closely resembles that of a truncated spherical droplet at thermodynamic equilibrium. At short times after which the droplet first comes into contact with the surface, t_c, however, the initially measured $\theta_{w,RS}$ is often not the true thermodynamic equilibrium contact angle, $\theta_{w,0}$. The measured $\theta_{w,RS}$ will approach $\theta_{w,0}$ given enough contact time, t_c, for the droplet to equilibrate with the surface. Given the discrepancy between $\theta_{w,RS}$ and $\theta_{w,0}$ at the experimentally practical short t_c's, the receding and advancing contact angles, $\theta_{w,R}$ and $\theta_{w,A}$ (Figure 1A and 1C), respectively, were measured to set the limits on $\theta_{w,0}$. For any given three-phase system, the true thermodynamic equilibrium contact angle, $\theta_{w,0}$, can take on any value between $\theta_{w,R}$ and $\theta_{w,A}$, with $\theta_{w,R} < \theta_{w,0} < \theta_{w,A}$.[37]

The range of the dynamic contact angles of a given system is commonly referred to as contact angle hysteresis (CAH) and can be quantified by calculating the difference between the cosines of the receding and advancing contact angles (which are proportional to the receding and advancing adhesion energies (eq 1), respectively) as follows:

$$\mathrm{CAH} = \cos\theta_{w,R} - \cos\theta_{w,A} \quad (2)$$

Because the true thermodynamic equilibrium contact angle can take on any value between the receding and advancing contact angles, a large CAH would imply large uncertainty in the expected wettability. Similarly, a small CAH implies little uncertainty in the expected wettability.

Figure 2A shows that in FW-CO the oil/water/rock system is slightly hydrophilic/oleophobic with water-receding $\theta_{w,RS}$ = 60°

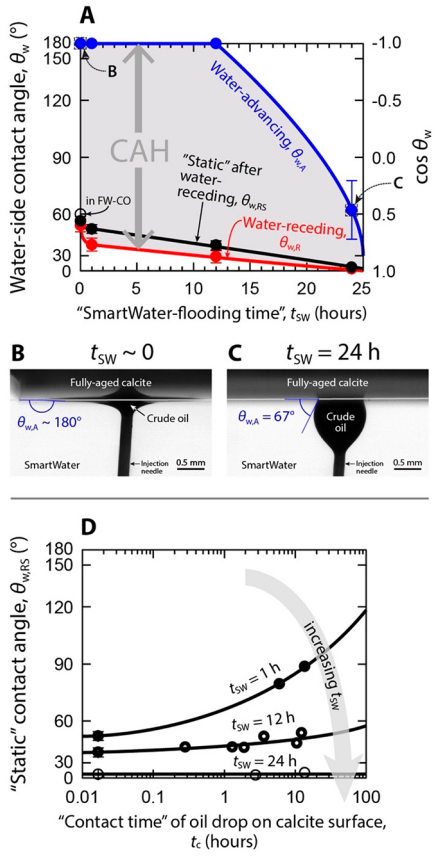

Figure 2. (A) Effect of the SmartWater flooding time, t_{SW}, (the amount of time that the fully aged calcite was exposed to SmartWater (10× diluted SW) at 100 °C) on the water-advancing contact angle ($\theta_{w,A}$; blue), static after water-receding contact angle ($\theta_{w,RS}$; black) measured after $t_c \approx 1$ min, and water-receding contact angle ($\theta_{w,R}$; red) of oil on SmartWater-flooded calcite in SmartWater. The open circle is for the reference case of fully aged calcite in FW-CO. The gray vertical arrow denotes contact angle hysteresis (CAH), as defined in the text (eq 2). The CAH region is highlighted by light-gray shading. (B and C) Snapshots of $\theta_{w,A}$ at $t_{SW} \approx 0$ and t_{SW} = 24 h, respectively. (D) Effect of oil-calcite contact time, t_c, during which the oil droplet was left in contact with the SmartWater-flooded calcite sample immersed in SmartWater at 23 °C, on $\theta_{w,RS}$ for fully aged calcite that was previously SmartWater-flooded for t_{SW} = 1 h (filled circles), 12 h (half-filled circles), and 24 h (unfilled circles). Each respective curve in panels A and D was drawn as a guide to the eye.

(measured after $t_c \approx 1$ min). Switching the aqueous solution from FW-CO to SmartWater (10× diluted SW) at 23 °C slightly increased the hydrophilicity/oleophobicity of the system to $\theta_{w,RS}$ = 56° (measured after $t_c \approx 1$ min; see Figure 2A). This effect occurred rapidly, within 15 min of switching the solutions. In both solutions (FW-CO and SmartWater), however, the oil droplet remained pinned (i.e., the oil/water/rock contact line did not move), resulting in advancing $\theta_{w,A}$ = 180° as the oil was completely withdrawn from the surface, and left behind a visible residual oil film (see Figure 2B).

Immersing the fully aged calcite in SmartWater at 100 °C for longer periods of time t_{SW} led to further increases in the water wetness of the oil/water/rock system (or, equivalently, decreases in $W_{o/w/r}$): $\theta_{w,A}$, $\theta_{w,RS}$, and $\theta_{w,R}$ all decreased as t_{SW} increased (Figure 2A), with

DOI: 10.1021/acs.langmuir.8b02711
Langmuir 2019, 35, 41−50

sharp decrease in $\theta_{w,R}$ and $\theta_{w,RS}$ at short times (t_{SW} < 1 h), followed by more gradual decrease thereafter.

Although $\theta_{w,R}$ and $\theta_{w,RS}$ both decreased, implying increased water wetness, the pinned oil/water/rock contact line leading to $\theta_{w,A}$ = 180° resulted in the high CAH for t_{SW} < 12 h, leading to uncertainty in the measured increased water wetness of the system and potential oil recovery. After t_{SW} > 12 h, however, the oil droplet was no longer completely pinned throughout a water advance: the oil/water/rock contact line of the oil droplet visibly moved on the calcite surface, the measured $\theta_{w,A}$ was <180°, and no thick oil film was left behind, indicating that the water wetness was significantly increased (see Figure 2C).

As shown in the gray-shaded region in Figure 2A, CAH first increased for t_{SW} < 12 h before decreasing after t_{SW} > 12 h. Noting that the maximum CAH for any system is 2 (Δcos θ_w units), at t_{SW} = 0 CAH increased from 1.5 in FW-CO to 1.6 in SmartWater. CAH then gradually increased to 1.9 at t_{SW} = 12 h. After 24 h of immersion in SmartWater (i.e., t_{SW} = 24 h), the CAH dramatically reduced to 0.5, which is a 3-fold reduction from the initial CAH at t_{SW} = 0 h.

In addition to studying the wettability of the system at short t_c's, knowing the thermodynamic equilibrium wettability of the system and the rate at which the system equilibrates toward its thermodynamic equilibrium state has implications for the optimum injection rate for SmartWater flooding (discussed further in Section 4.1). To gain insight into the thermodynamic equilibrium wettability of the oil/water/rock system after SmartWater flooding, static after water-receding contact angles, $\theta_{w,RS}$, were also measured after different contact times, t_c, over which the oil droplet was left in contact at 23 °C with the fully aged calcite surfaces that were previously immersed in SmartWater at 100 °C for the different SmartWater flooding times, t_{SW} (discussed in the preceding paragraphs). Note that since topographical changes to the calcite surface due to exchanging solutions occur much slower at 23 °C than at >75 °C (Section 4.3), it can be inferred that the calcite surface structure/roughness did not change (considerably) over the period during which the oil droplet was left in contact with the calcite surface at 23 °C. Therefore, any observed changes in $\theta_{w,RS}$ during the contact time experiments were due to the oil droplet equilibrating toward the thermodynamic equilibrium $\theta_{w,0}$.

Figure 2D shows that for t_{SW} = 1 h, $\theta_{w,RS}$ increased significantly from 51 to 89° with the droplet continually spreading on the calcite surface over the t_c = 13.6 h oil/rock contact time, indicating that the thermodynamic equilibrium wettability of the system is significantly less water-wet than the instantaneous one. However, the extent of the increase in $\theta_{w,RS}$ over increasing t_c decreased as the calcite was immersed in SmartWater for increasingly longer periods of time (i.e., increasing t_{SW}). For the calcite surface that had been immersed in SmartWater for t_{SW} = 24 h, the oil droplet did not continually spread on the calcite surface and $\theta_{w,RS}$ remained unchanged even after t_c > 12 h. In this case, the system established its thermodynamic equilibrium wettability state instantaneously (i.e., t_c of a few minutes).

3.2. In Situ Dynamic Absolute Asperity Height Changes of the Calcite Surface Due to SmartWater Flooding, Measured Using the SFA. The topography and combined thickness of two apposing calcite surfaces were monitored over time using an SFA under mimicked reservoir conditions of both the aging period and the SmartWater flooding period to study the effect of SmartWater flooding on the morphology of the calcite surface. The in situ SFA measurements were performed at 75 ± 5 °C during both the aging and SmartWater flooding periods.

Figure 3 shows how the FECO fringes (used to visualize and calculate thickness) from a typical SFA experiment evolved with time for calcite in FW-CO and subsequently in SmartWater (10× diluted SW) at 75 ± 5 °C. The changes in the combined calcite thickness, ΔH, were determined relative to the combined calcite thickness in dry air: H = 55 nm (Figure 3A). The injection of FW-CO marked the starting time t = 0, after which the calcite surface thickness was monitored throughout the aging and the subsequent SmartWater flooding times. The temporal evolution of the thickness changes of the combined calcite films in FW-CO and SmartWater based on

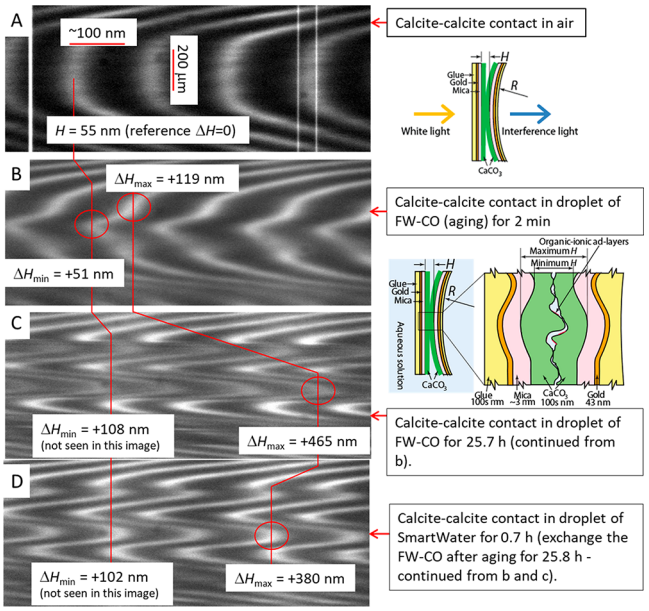

Figure 3. FECO fringes showing the temporal evolution of calcite surface morphology at 75 ± 5 °C going from (A) calcite in air to (B and C) calcite submerged in FW-CO to (D) replacing FW-CO with SmartWater (10× diluted SW). FECO fringes were used to calculate the maximum and minimum calcite thicknesses, ΔH_{max} and ΔH_{min}, respectively, with the corresponding schematics of the surface profiles in the right-side panels. Red circles indicate the positions along the FECO line from which ΔH_{max} and ΔH_{min} were calculated. For panels C and D, ΔH_{min} was obtained from another FECO frame and therefore was not circled (as noted).

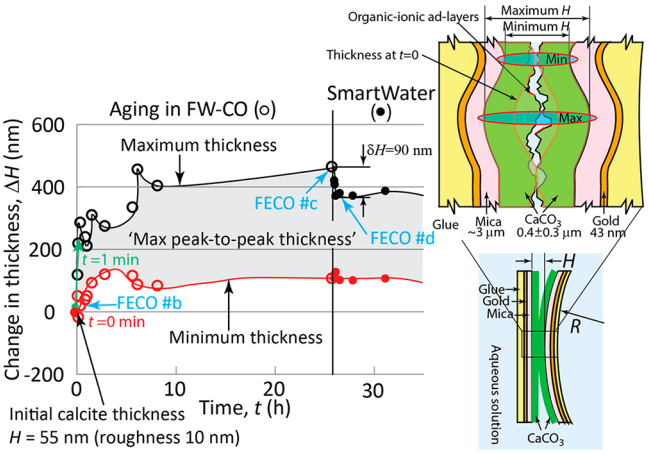

Figure 4. Temporal evolution of calcite thicknesses, ΔH, during aging and the subsequent SmartWater flooding at 75 ± 5 °C. The representative FECO fringes are shown in Figure 3 at indicated time points. "FECO #b", "FECO #c", and "FECO #d" refer to the representative FECO fringes during the experiment shown in the correspondingly labelled panels of Figure 3.

FECO fringe analyses is shown in Figure 4. Experiments were also performed using SW to mimic the conventional water flooding process in carbonate fields; the corresponding results are reported in Figure S4.

Aging in FW-CO increased the thickness and roughness of the calcite surfaces. Within 1 min after injecting FW-CO for the aging of the initially smooth calcite surfaces (Figure 3A), both the minimum, ΔH_{min}, and maximum, ΔH_{max}, calcite thicknesses abruptly increased by +51 and +119 nm (Figure 4), respectively, indicating that material was added to the surfaces. Complementary topography measurements

DOI: 10.1021/acs.langmuir.8b02711
Langmuir 2019, 35, 41−50

using the atomic force microscope (AFM) also confirmed this observation of material buildup (Section SI S3.2.1). In situ AFM measurements scanning the surface topography while the calcite surface was immersed in the FW-CO solution at 50 °C showed that an ∼100-nm-thick material was nonuniformly added to the calcite surface after 20 min of immersing the initially smooth calcite surface in FW-CO (cf. Figure S5A,B). Material removal (e.g., via dissolution) also occurred during aging, as noted by the minimum calcite thickness decreasing by $\delta H_{min} = -40$ nm. At the end of the aging stage ($t \approx 26$ h), roughening and precipitation developed further, resulting in an overall increased $\Delta H_{min} = +108$ nm and $\Delta H_{max} = +465$ nm, as seen in the jagged FECO fringes in Figure 3C.

SmartWater flooding thereafter decreased the thickness of the fully aged calcite surfaces. Immediately after FW-CO was exchanged with SmartWater (i.e., SmartWater flooding), ΔH_{max} decreased sharply by $\delta H_{max} = -85$ nm from +465 to +380 nm within a few minutes. During the same period, ΔH_{min} did not vary. This indicated that a ∼100 nm film (ad-layer) was removed from the fully aged surface (as flakes) (Figure 3D). This film layer removal exposed an underlying surface that is still roughened, in comparison to the initially smooth preaged calcite surfaces, as seen in the FECO fringes shown in Figure 3D.

Note that the roughness (i.e., the maximum peak-to-peak thickness, $\Delta H_{max} - \Delta H_{min}$) within the contact area varied dramatically throughout both the aging and SmartWater flooding processes, at timescales ranging from minutes to hours. SmartWater flooding rapidly (within a few minutes) decreased the maximum peak-to-peak thickness by hundreds of nanometers. As a visual example showing the variation in roughness within the contact area, selective scans of FECO fringes across the contact area after the calcite surfaces had been aged in FW-CO for 10 min are shown in Figure S3. At this time point, ΔH_{min} and ΔH_{max} were found within the center part of the contact area, with $\Delta H_{min} = -40$ nm (due to dissolution) and $\Delta H_{max} = +245$ nm (due to precipitation of salts and dissolved calcite from the solution). However, as illustrated by the FECO fringes shown in Figure S3B−G, note the variation in the surface topography away from the center (but still within the contact area). In these areas, away from the center contact area, pits and peaks of the calcite surfaces were observed. Furthermore, also in these areas, where the calcite surfaces were not deformed, the FECO fringes were broader than those of calcite surfaces in air (due to the refractive index mismatch between water and calcite; for more details see SI Section S3.2 after Figure S3), indicating that lateral submicrometer-scale roughening was occurring even well away from where the surfaces were in contact (cf. the FECO fringes ∼200 μm away from the contact boundary in Figure S3B,G that are parabolic-shaped, similar to the FECO fringe shape of separated surfaces).

3.3. Studies Using Reservoir Carbonate Samples and Physicochemical Characterizations Using SEM-EDS. To determine the applicability of our findings using model calcite surfaces to actual reservoir rocks, topographical and physicochemical changes in reservoir carbonate samples due to aging and SmartWater flooding using 10× diluted SW were studied using SEM-EDS. Representative SEM images of the reservoir carbonate samples that were (A) oil-free, (B) fully aged, and (C) SmartWater-flooded for $t_{SW} = 48$ h are shown in Figure 5. The same location (within 100 μm) is depicted in each image. The corresponding elemental compositions of each sample characterized using EDS are reported in Figure S7.

These experiments using reservoir carbonate samples showed similar physicochemical changes due to aging and SmartWater flooding that were reported by Chen et al.[21] for experiments using polished single-crystalline calcite surfaces. The oil-free reservoir carbonate sample (Figure 5A) exhibited a granular structure with pores that are approximately 1 μm in diameter along the surface. It is important to note that dolomite existed as individual grains within the reservoir carbonate sample. After aging, an ad-layer composed of organic and ionic species formed on the surface, as seen in Figure 5B, where the granular structure had been obscured and large NaCl crystals (highlighted in the yellow circle in Figure S8B) had also precipitated on the surface. The red circle in Figure S8B highlights the reservoir carbonate sample surface covered with an organic−ionic

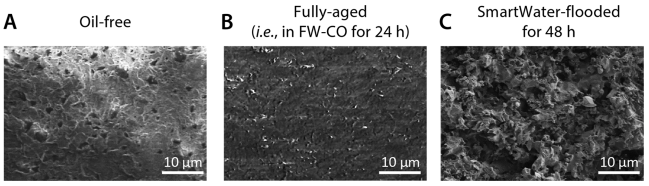

Figure 5. SEM images of reservoir carbonate samples that were treated at 100 °C that are (A) oil-free (extracted reservoir carbonate sample cleaned with toluene to remove organic/oil components), (B) fully aged, and (C) SmartWater-flooded using 10× diluted SW at 100 °C for 48 h. Prior to imaging, each sample was cooled and gently removed from the salt water solution, gently washed with DI water (to remove the salts precipitated from the salt water solution), and gently dried with nitrogen gas. This was done to minimize the effects of SEM vacuum pressure on precipitating salts onto the sample surfaces. Note that the initially porous rock structure (seen in panel A) was almost completely covered after aging under reservoir conditions (panel B). Exposure to SmartWater resulted in significant dissolution and removal of the adsorbed surface layer, exposing a new porous and roughened rock structure (panel C).

layer, which is lighter due to the low conductivity of organic species. The ad-layer appeared as a porous mesh, which would allow salt water solutions to access the underlying calcite. The presence of the salts and organic layer is consistent with the previous observations made for the formation of a surface layer on polished calcite surfaces after aging, as discussed in the Introduction. After SmartWater flooding (Figure 5C), most of the adsorbed organic layer and ionic salts were no longer present, and the surface topography appeared roughened compared to the initial oil-free reservoir carbonate sample surface, presumably due to detachment of the ad-layer, dissolution, and precipitation. Further magnification of Figure 5C (Figure S9) showed that some areas of the reservoir carbonate sample surface were still covered with an adsorbed organic layer and salts even after SmartWater flooding for $t_{SW} = 48$ h. This indicated that not all of the adsorbed organic−ionic layer was completely removed by SmartWater in some areas.

4. DISCUSSION

4.1. Timescales of the SmartWater Effect. Our dynamic contact angle results show that the oil/water/rock water wetness increases significantly over time after FW-CO is replaced with SmartWater (as occurs during SmartWater flooding IOR). We find that the increase in water wetness, which could potentially increase the oil recovery, is due to multiple effects that are characterized by at least two different timescales: (1) short ($t_{SW} < 15$ min) and (2) long ($t_{SW} > 12$ h).

On a short timescale of $t_{SW} < 15$ min, the initial rapid, but slight, increase in the oil/water/rock water wetness (modest decrease in $\theta_{w,RS}$; see Figure 2) due to SmartWater flooding is a result of the rapid increase in the electrostatic double-layer (EDL) repulsion (there is still van der Waals adhesion) between the oil and rock surfaces across the salt water film,[21] which decreases the oil/water/rock adhesion energy $W_{o/w/r}$ according to the well-established extended Derjaguin−Landau−Verwey−Overbeek (DLVO) theory[22] (Figure 6). This increases the oil/water/rock water wetness, implying an increase in oil recovery. We note that on this short timescale, $t_{SW} < 15$ min, there are no observable roughness changes. Up to $t_{SW} = 12$ h, however, the pinned (immobile) oil/water/rock contact line, resulting in $\theta_{o,R} = 0°$ (and, equivalently, $\theta_{w,A} = 180°$) and leaving behind a thick, visible, residual oil film on the surface, implies low oil recovery. The decreased water-receding $\theta_{w,R}$ and the pinned water-advancing contact line (and therefore high water-advancing $\theta_{w,A}$) together result in the

DOI: 10.1021/acs.langmuir.8b02711
Langmuir 2019, 35, 41−50

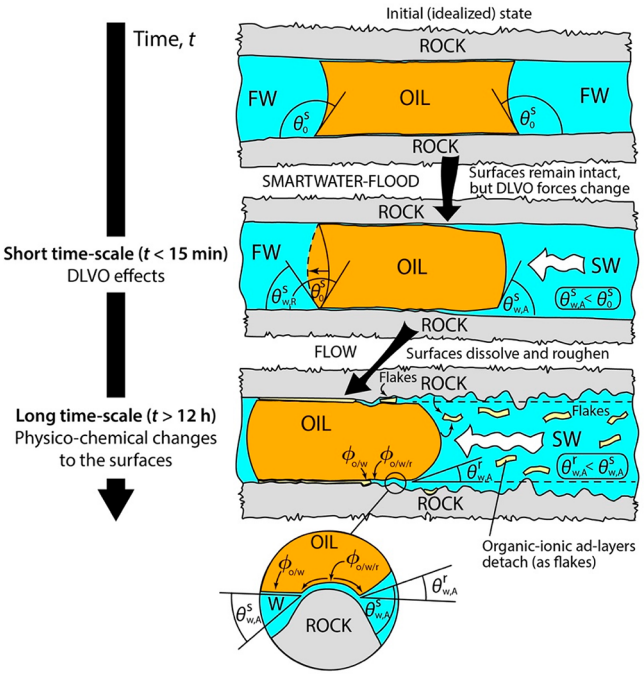

Figure 6. Proposed mechanism of the SmartWater effect for improving oil recovery in oil/water/rock interfaces from exchanging reservoir formation water (FW) with SmartWater (SW), wherein processes that occur on two distinct timescales that impact the oil/water/rock wettability can be observed. The first timescale involves changes in the physical surface (colloidal) interaction forces on the initially smooth surfaces (as denoted by the s superscript), which lead to lower advancing and receding contact angles ($\theta^s_{w,A}$ and $\theta^s_{w,R}$, respectively) in comparison to the initial contact angle in FW, θ^s_0. The second timescale involves the removal of ad-layers as flakes and surface dissolution and roughening, which decrease the oil/water/rock and increase the oil/water contact areas by factors of $\phi_{o/w/r}$ and $\phi_{o/w}$, respectively. These physicochemical changes lead to dramatic decreases in the advancing and receding contact angles ($\theta^r_{w,A}$ and $\theta^r_{w,R}$, respectively) on the now roughened surfaces (as denoted by the r superscript).

increasing CAH at t_{SW} < 15 min (and up to t_{SW} = 12 h). Large CAH implies high uncertainty in measuring the thermodynamic equilibrium wettability (as also seen from the significant increase in $\theta_{w,RS}$ as the oil droplet was left in contact with the calcite surface for long t_c to equilibrate to the thermodynamic equilibrium contact angle). Large CAH also implies that rate effects (such as the injection rate in SmartWater flooding IOR operations) would significantly affect oil recovery for SmartWater-flooded oil/water/rock systems not yet at thermodynamic equilibrium (further discussion to follow).

At longer times (t_{SW} > 12 h), the dramatic increase in the oil/water/rock water wetness, as observed by the significant decrease in the water-side contact angles and the depinning of the oil/water/rock contact line as the aqueous phase is advanced (Figure 2), can be attributed to the (slower) physicochemical changes of the mineral surface resulting from exposure to the SmartWater solution. These physicochemical changes begin to occur as early as a couple of minutes after exchanging the solutions but take on the order of >24 h to complete for the dramatic effects on wettability to be observed (Sections 3.1−3.3).

As discussed in Section 3.2, the SFA (Figure 4) results show that exposing the fully aged calcite surface to SmartWater leads to significant removal of material from the surface. The material that is removed from the calcite surface is the patchy organic−ionic ad-layers (removed as flakes) that were reported by Chen et al.[21] (Introduction). The detachment of the surface ad-layer exposes a roughened underlying calcite that was initially smooth (Figure 6). The ad-layer is removed as a result of the SmartWater penetrating the thin aqueous film between the ad-layer and the rock and dissolving and roughening the underlying rock surface (discussed further in Section 4.2). These effects lead to the detachment of the ad-layers and also result in a rock surface that is rougher on the nano- and microscales compared to the roughness of the organic−ionic ad-layers (Figures 3−5).

The removal of the patchy organic−ionic ad-layers removes the oil-wet (hydrophobic) organics from the calcite surface and exposes the more water-wet (hydrophilic) calcite underneath, resulting in the much reduced $W_{o/w/r}$, lower θ_w, and, more importantly, the depinning of the oil/water/rock contact line as water advances on the surface. The mobile oil/water/rock contact line would significantly increase the amount of oil recovered. In addition, the roughening of the underlying calcite surface results in further reductions in the effective $W_{o/w/r}$ and θ_w, which result in further increased oil removal. This roughening-induced enhanced water wettability is due to the decreases in the oil/water/rock contact area and the increases in the oil/water contact area by factors of $\phi_{o/w/r}$ and $\phi_{o/w}$, respectively (Figure 6). These changes to the interfacial contact areas in turn decrease the effective $W_{o/w/r}$ ($W_{o/w/r,effective}$), which thereby decrease the contact angle θ^r_w on the rough (denoted by the r superscript) surface and increase the water wetness, in comparison to the water-side contact angle on the smooth (denoted by the s superscript) surface, θ^s_w.[26−29] These roughening-induced effects also result in the dramatic reduction of the CAH, which is also apparent from the negligible change in $\theta_{w,RS}$ even after long oil/calcite contact (equilibration) times, leading to less variability in measuring the thermodynamic equilibrium oil/water/rock wettability.

Additionally, as the flakes detach from the rock surface, they drag and remove oil with them, further increasing oil recovery directly. Previous results[21] showed that the flakes appear to be charge-neutral with very weak interactions with other flakes, while oil is attached to the organic components of the flakes. Furthermore, the removed organic−ionic flakes are on the order of a millimeter squared area with about 100 nm thickness, providing the flakes with enough stiffness to not curl up in solution and not conform to the new topography of the roughened rock surface. This stiffness results in a decreased interaction contact area for the colloidal interactions and adhesion between the flakes and the rock, which require nanometer-scale proximity. As such, with the ongoing roughening, the adhesion becomes overpowered by the forces due to liquid flow, and the flakes, together with oil, detach.

Our CAH results suggest that there is a minimum amount of SmartWater flooding time, $t_{SW,min}$, (or a maximum rate of SmartWater injection) on the order of t_{SW} > 24 h that the rock surfaces on the laboratory scale need to be exposed to the SmartWater for the SmartWater to be effective in releasing oil from the surface. For t_{SW} < 24 h, the large CAH and the large decrease in oil/water/rock water wetness at increasing oil/rock contact times suggest that the rate of SmartWater injection (i.e., the retention time) could significantly affect oil release. This is a result of the patchy organic−ionic layers not having

DOI: 10.1021/acs.langmuir.8b02711
Langmuir 2019, 35, 41−50

sufficient time to detach and the underlying calcite surface not having sufficient time to dissolve and roughen. For $t_{SW} > 24$ h $> t_{SW,min}$, the rate of SmartWater injection would be such that these processes will have sufficient time to be completed, resulting in less variability in the oil/water/rock wettability and decreased CAH. This should lead to more consistent improved oil release from SmartWater flooding, independent of the rate of SmartWater injection.

4.2. Explanation of the Physicochemical Changes in the Mineral Surface Due to SmartWater Flooding. Our experimental results show that SmartWater flooding detaches preadsorbed organic−ionic patchy ad-layers that were formed during aging (as flakes[21]) and roughens the underlying initially smooth calcite surface underneath (Figures 3−5 and S5). The ad-layer removal is in part due to calcite dissolution as the solution becomes significantly undersaturated with calcite upon exchanging the solution from FW-CO to SmartWater (10× diluted SW). Referring to Table 3 (Section 2.1.1), where species that are undersaturated have SI < 0, there is 300× less calcium and 30× less carbonate ions in SmartWater, compared to FW-CO. For undersaturated solutions, the dissolution of calcium carbonate minerals (e.g., calcite) proceeds through the following reaction pathway

$$H^+(aq) + CaCO_3(s) \xrightarrow{k_1} Ca^{2+}(aq) + HCO_3^-(aq) \quad (3)$$

$$HCO_3^-(aq) + H^+(aq) \overset{K}{\leftrightarrow} H_2CO_3(aq) \xrightarrow{k_2} CO_2(aq) + H_2O(l) \quad (4)$$

where k_1 and k_2 are the relevant rate constants and K is the equilibrium constant.[38]

The higher degree of undersaturation of calcite and other calcium-containing minerals (Table 3) enhances calcite dissolution and results in the release of the ad-layers; however, as calcite dissolves in the confined interface of the ad-layer/calcite interface, the local concentration of carbonate ions can dramatically increase due to transport limitations. As the concentration of carbonate ions increases, reprecipitation (e.g., crystallization) can occur as other carbonate-containing minerals precipitate onto the surface. Because of the reactivity of the sulfate ions[13,39] present, the formation of anhydrite and gypsum can occur as follows

$$Ca^{2+}(aq) + SO_4^{2-}(aq) + 2H_2O(l) \xrightarrow{k_3} CaSO_4{\cdot}2H_2O(s) \quad (5)$$

where k_3 is the relevant rate constant.[38] These products are relatively insoluble in the confined interface, and thus the sulfate-containing carbonate minerals precipitate onto the surface; however, the precipitation is limited due to the equilibrium established in the solution as diffusion occurs. The combination of mineral dissolution and reprecipitation results in roughening of the calcite surfaces.

These physicochemical changes occur much slower than the rapid increase in the EDL repulsion in part due to material transport limitations. As seen from the SFA results, while exchanging FW-CO with SmartWater resulted in a rapid drop in the maximum thickness δH_{max} of −85 nm within a few minutes with the release of the ad-layers (Figure 4; similar to the results obtained in the experiments using SW as the SmartWater flooding salt water (Figure S4)), however, the released ad-layers that were still in close proximity to the calcite surfaces prevented the thinning of the underlying calcite surfaces for 4 to 5 h (Figure 4).

4.3. Temperature Effects. Elevated temperature and the presence of crude oil components in the formation water increase the rate of chemical reactions, such as the dissolution and roughening of the calcite surface, even though the solubility of calcite is lower at higher temperatures. Previous AFM results show that dissolution, precipitation, and restructuring of calcite surfaces in FW are significantly more pronounced at 40−50 °C than at 25 °C.[21] The limited dissolution and (re)precipitation of calcite at room temperature (i.e., 23 °C) in FW were confirmed with SFA measurements (Figure S6). Adding water-soluble components of crude oil, such as the organic acid components of the oil, and elevating the temperature to 75 °C enhance both the rate and magnitude of calcite roughening through both dissolution and precipitation (Figure S6). Asphaltenes contain reactive groups that can initiate the dissolution of calcite as well as speed up the dissolution through acidic groups that locally lower the pH near the calcite surface. The dissolved calcium and carbonate ions can (re)precipitate elsewhere as well as together with salts from the injection SmartWater. The extent of the detachment of the ad-layers (Figure 6) and mineral dissolution increases with increasing SmartWater flooding time t_{SW} until the solution becomes saturated at equilibrium.

4.4. Implications for Oil Reservoir Rocks. Our experiments with reservoir carbonate samples show that the same processes that comprise the SmartWater effect occur for both initially smooth crystalline calcite samples and rough reservoir carbonate samples. From these findings, we conclude that the aging and SmartWater flooding processes affect smooth crystalline calcite in the same way that they affect reservoir carbonate rock, except that roughness changes are more pronounced with smooth calcite. From this, we can infer that the magnitude of the changes in the effective adhesion energy $W_{o/w/r,effective}$ and wettability due to SmartWater flooding in carbonate reservoirs is expected to be qualitatively similar to the effects measured for the smooth crystalline calcite samples.

4.5. Possible Implications for Field Studies. The front of the injection flooding water is estimated to move by 1 ft a day in the oil field.[34] At such low velocities, ion diffusion will increase the concentration (salinity) of the flooding water at the flooding front to values similar to that of formation water (FW). However, continuous SmartWater flooding will generate a decreasing salinity concentration gradient at the flood front that mixes with the FW in the reservoir. It may take days or months before a region within the reservoir reaches the same salinity as the flooding water, in contrast to seconds in the laboratory experiments presented here. The processes of releasing the organic−ionic layer and surface roughening, as well as the reduction of the colloidal interactions, together resulting in a reduction in the adhesion energy of the rock/oil interface, are postulated to be the same for both laboratory experiments and field reservoir SmartWater flooding. Directly scaling up the findings from our laboratory experiments to field studies by performing core flooding and/or field test studies is a natural next step but is beyond the scope of this work.

The oil within the reservoir rock is trapped in a porous network with pore diameters typically on the micrometer (or even millimeter or larger in water-wet systems) scale. The slow velocity of the flooding water front reduces the possibility of water (viscous) fingering (or percolating) through the reservoir rock. In the case where water fingering occurs, only the water would be pushed through, leaving the oil behind. Thus, as long as there is no water fingering, then the applied

DOI: 10.1021/acs.langmuir.8b02711
Langmuir 2019, 35, 41−50

pressure (from the injection water) on the oil at the flooding front is about the same as the pressure further back in the decreased-salinity zone. The oil released from the decreased-salinity zone is therefore pushed toward the oil well(s).

5. CONCLUSIONS

Exchanging formation water with SmartWater (as occurs during SmartWater flooding or, synonymously, low-salinity water or diluted seawater flooding IOR) improves oil recovery by significantly decreasing the effective oil/water/carbonate rock adhesion energy over time, which thereby increases the water wetness. We find that the effects of SmartWater on increasing water wetness, thereby improving oil recovery, are characterized by at least two distinct characteristic time scales: (1) short (t_{SW} < 15 min), during which the physical electric double-layer repulsive forces between the oil and rock surface across the salt water film increases rapidly; and (2) long (t_{SW} > 12 h to complete), during which physicochemical changes to the rock surface occur as a result of calcite dissolution due to the undersaturation of calcite in the SmartWater solution. The longer timescale physicochemical changes include the detachment of preadsorbed organic−ionic ad-layers formed during aging and nanometer-scale roughening of the initially smooth(er) rock surface underneath. The detachment of the organic−ionic ad-layers directly removes oil and oil-wet (hydrophobic) organics and reveals the more water-wet (hydrophilic) rock surface underneath. For both types of surfaces that were studied, namely, the model calcite surfaces and the reservoir carbonate samples, the reduction in adhesion energy is largely due to the slower physicochemical changes to the rock surface. Although the short timescale changes to the physical colloidal interaction forces decrease the oil/water/rock adhesion energy (which increases the water wetness), it is not until after the much longer timescale physicochemical changes to the rock surface that the effective adhesion energy is significantly reduced, water wetness is significantly increased, and oil is released from the surfaces, leading to improved oil recovery. An important result from this and previous[21] work is the discovery of 50−100-nm-thick organic−ionic ad-layers that separate the oil and calcite surfaces in the reservoir, whose detachment helps release the oil from the calcite due to the increase in the hydrophilic nature of the fully aged calcite surface. A key implication of this result is that oil composition (e.g., acidity and types of water-soluble asphaltenes) may control the formation and nature of the ad-layers. Depending on the oil composition, the SmartWater effect on oil recovery might be weak where the ad-layer is poorly developed, compared to other systems where the oil composition results in an ad-layer that is much more robust. In such systems, SmartWater flooding could have a marked effect on the removal of the ad-layer, consequently increasing the water wetness for enhanced oil recovery.

■ ASSOCIATED CONTENT

Supporting Information

The Supporting Information is available free of charge on the ACS Publications website at DOI: 10.1021/acs.langmuir.8b02711.

Preparation procedure for synthesized calcite ($CaCO_3$); XRD analysis of carbonate reservoir rock sample; justification of our aging procedure; AFM imaging of calcite samples in situ during changing solutions; surface forces apparatus experiments; AFM studies of dynamic (time-dependent) topographical changes of calcite from changing solution conditions, imaging calcite samples in situ; and topographical and chemical changes in the reservoir carbonate samples (PDF)

■ AUTHOR INFORMATION

Corresponding Author

*E-mail: szuying@ucsb.edu.

ORCID

Szu-Ying Chen: 0000-0003-3486-9698
Kai Kristiansen: 0000-0002-7555-9437
Howard A. Dobbs: 0000-0002-6853-9278
Yair Kaufman: 0000-0001-7771-8502
Jacob N. Israelachvili: 0000-0001-8915-8741

Present Addresses

[⊥]Now at the Department of Chemical Engineering, Brigham Young University, Provo, Utah 84606, United States.
[#]Now at the Zuckerberg Institute for Water Research, The Jacob Blaustein Institutes for Desert Research, Ben Gurion University of the Negev, Sede Boqer Campus 84990, Midreshet Ben-Gurion, Israel.

Notes

The authors declare no competing financial interest.

■ ACKNOWLEDGMENTS

This work was supported by a grant from the Saudi Arabian Oil Company (Saudi Aramco). H.A.D. was supported by the Department of Energy, Office of Basic Energy Sciences, Division of Materials Sciences and Engineering, under award no. DE-FG02-87ER-45331 (development and fabrication of thin calcite films). MRL Shared Experimental Facilities were used in this study and are supported by the MRSEC Program of the NSF under award no. DMR 1121053, a member of the NSF-funded Materials Research Facilities Network (www.mrfn.org). The authors also kindly acknowledge the anonymous reviewers for their numerous constructive comments.

■ REFERENCES

(1) McGuire, P. L.; Chatham, J. R.; Paskvan, F. K.; Sommer, D. M.; Carini, F. H. *Low Salinity Oil Recovery: An Exciting New EOR Opportunity for Alaska's North Slope*. Paper SPE 93903 presented at the 2005 SPE Western Regional Meeting held in Irvine, California, USA, 30 March−1 April, 2005.

(2) Seccombe, J.; Lager, A.; Jerauld, G.; Jhaveri, B.; Buikema, T.; Bassler, S.; Denis, J.; Webb, K.; Cockin, A.; Fueg, E. *Demonstration of Low-Salinity EOR at Interwell Scale, Endicott Field, Alaska*. Paper SPE 129692 presented at the 2010 SPE Improved Oil Recovery Symposium held in Tulsa, Oklahoma, USA, 24−28 April, 2010.

(3) Webb, K. J.; Black, C. J. J.; Al-Ajeel, H. *Low Salinity Oil Recovery - Log-Inject-Log*. Paper SPE 89379 presented at the SPE/DOE 14th Symposium on Improved Oil Recovery held in Tulsa, Oklahoma, USA, 17−21 April, 2004.

(4) Webb, K. J.; Black, C. J. J.; Edmonds, L. J. *Low Salinity Oil Recovery: The Role of Reservoir Condition Corefloods*. Presented at the 13th European Symposium on Improved Oil Recovery held in Budapest, Hungary, 25−27 April, 2005.

(5) Austad, T.; Strand, S.; Høgnesen, E. J.; Zhang, P. *Seawater as IOR Fluid in Fractured Chalk*. Paper SPE 93900 presented at the SPE International Symposium on Oilfield Chemistry held in Houston, Texas, USA, 2−4 February, 2005.

(6) Webb, K. J.; Black, C. J. J.; Tjetland, G. *A Laboratory Study Investigating Methods for Improving Oil Recovery in Carbonates*. Paper

DOI: 10.1021/acs.langmuir.8b02711
Langmuir 2019, 35, 41−50

IPTC 10506 presented at International Petroleum Technology Conference held in Doha, Qatar, 21−23 November, 2005.
(7) Chandrasekhar, S.; Mohanty, K. K. *Wettability Alteration with Brine Composition in High Temperature Carbonate Reservoirs*. Paper SPE 166280 presented at the SPE Annual Technical Conference and Exhibition held in New Orleans, Louisiana, USA, 30 September−2 October, 2013.
(8) Gupta, R.; Mohanty, K. K. Wettability Alteration Mechanism for Oil Recovery From Fractured Carbonate Rocks. *Transp. Porous Media* **2011**, *87* (2), 635−652.
(9) Yousef, A. A.; Liu, J. S.; Blanchard, G. W. *Smart Waterflooding: Industry's First Field Test in Carbonate Reservoirs*. In Paper SPE 159526 presented at the SPE Annual Technical Conference and Exhibition held in San Antonio, Texas, USA, 8−10 October, 2012.
(10) Seethepalli, A.; Adibhatla, B.; Mohanty, K. K. Physicochemical Interactions During Surfactant Flooding of Fractured Carbonate Reservoirs. *SPE Journal* **2004**, *9* (4), 411−418.
(11) Lu, J.; Goudarzi, A.; Chen, P.; Kim, D. H.; Delshad, M.; Mohanty, K. K.; Sepehrnoori, K.; Weerasooriya, U. P.; Pope, G. A. Enhanced Oil Recovery From High-Temperature, High-Salinity Naturally Fractured Carbonate Reservoirs by Surfactant Flood. *J. Pet. Sci. Eng.* **2014**, *124*, 122−131.
(12) Iglauer, S.; Wu, Y.; Shuler, P.; Tang, Y.; Goddard, W. A., III. New Surfactant Classes for Enhanced Oil Recovery and Their Tertiary Oil Recovery Potential. *J. Pet. Sci. Eng.* **2010**, *71* (1−2), 23−29.
(13) Gupta, R.; Smith, P. G., Jr.; Hu, L.; Willingham, T. W.; Cascio, L. M.; Shyeh, J. J.; Harris, C. R. *Enhanced Waterflood for Middle East Carbonate Cores − Impact of Injection Water Composition*. Paper SPE 142668 presented at the SPE Middle East Oil and Gas Show and Conference held in Manama, Bahrain, 25−28 September, 2011.
(14) Nwidee, L. N.; Theophilus, S.; Barifcani, A.; Sarmadivaleh, M.; Iglauer, S. EOR Processes, Opportunities and Technological Advancements. In *Chemical Enhanced Oil Recovery (cEOR) - A Practical Overview* [Online]; Romero-Zeron, L., Ed.; InTech, 2016; Chapter 1, pp 2−52. https://www.intechopen.com/books/chemical-enhanced-oil-recovery-ceor-a-practical-overview/eor-processes-opportunities-and-technological-advancements (accessed July 27, 2017).
(15) Myint, P. C.; Firoozabadi, A. Thin Liquid Films in Improved Oil Recovery From Low-Salinity Brine. *Curr. Opin. Colloid Interface Sci.* **2015**, *20*, 105−114.
(16) Yildiz, H. O.; Morrow, N. R. Effect of Brine Composition on Recovery of Moutray Crude Oil by Waterflooding. *J. Pet. Sci. Eng.* **1996**, *14* (3−4), 159−168.
(17) Lager, A.; Webb, K. J.; Black, C. J. J.; Singleton, M.; Sorbie, K. S. Low Salinity Oil Recovery − An Experimental Investigation. *Petrophysics* **2008**, *49* (1), 28−35.
(18) Mugele, F.; Siretanu, I.; Kumar, N.; Bera, B.; Wang, L.; de Ruiter, R.; Maestro, A.; Duits, M.; van den Ende, D.; Collins, I. Insights From Ion Adsorption and Contact-Angle Alteration at Mineral Surfaces for Low-Salinity Waterflooding. *SPE J.* **2016**, *21* (4), 38−48.
(19) Morrow, N. R.; Tang, G.-Q.; Valat, M.; Xie, X. Prospects of Improved Oil Recovery Related to Wettability and Brine Composition. *J. Pet. Sci. Eng.* **1998**, *20* (3−4), 267−276.
(20) Tang, G.-Q.; Morrow, N. R. Influence of Brine Composition and Fines Migration on Crude Oil/Brine/Rock Interactions and Oil Recovery. *J. Pet. Sci. Eng.* **1999**, *24*, 99−111.
(21) Chen, S.-Y.; Kaufman, Y.; Kristiansen, K.; Seo, D.; Schrader, A. M.; Alotaibi, M. B.; Dobbs, H. A.; Cadirov, N. A.; Boles, J. R.; Ayirala, S. C.; Israelachvili, J. N.; Yousef, A. A. Effects of Salinity on Oil Recovery (the "Dilution Effect"): Experimental and Theoretical Studies of Crude Oil/Brine/Carbonate Surface Restructuring and Associated Physicochemical Interactions. *Energy Fuels* **2017**, *31* (9), 8925−8941.
(22) Israelachvili, J. N. *Intermolecular and Surface Forces*, 3rd ed.; Academic Press: London, 2011.
(23) Hirasaki, G. J. Wettability: Fundamentals and Surface Forces. *SPE Form. Eval.* **1991**, *6* (2), 217−226.
(24) Mugele, F.; Bera, B.; Cavalli, A.; Siretanu, I.; Maestro, A.; Duits, M.; Cohen-Stuart, M.; van den Ende, D.; Stocker, I.; Collins, I. Ion Adsorption-Induced Wetting Transition in Oil-Water-Mineral Systems. *Sci. Rep.* **2015**, *5*, 10519.
(25) Alcantar, N.; Israelachvili, J. N.; Boles, J. Forces and Ionic Transport Between Mica Surfaces: Implications for Pressure Solution. *Geochim. Cosmochim. Acta* **2003**, *67* (7), 1289−1304.
(26) Hiorth, A.; Cathles, L. M.; Madland, M. V. The Impact of Pore Water Chemistry on Carbonate Surface Charge and Oil Wettability. *Transp. Porous Media* **2010**, *85* (1), 1−21.
(27) Kaufman, Y.; Chen, S.-Y.; Mishra, H.; Schrader, A. M.; Lee, D. W.; Das, S.; Donaldson, S. H., Jr.; Israelachvili, J. N. Simple-to-Apply Wetting Model to Predict Thermodynamically Stable and Metastable Contact Angles on Textured/Rough/Patterned Surfaces. *J. Phys. Chem. C* **2017**, *121* (10), 5642−5656.
(28) Cassie, A. B. D.; Baxter, S. Wettability of Porous Surfaces. *Trans. Faraday Soc.* **1944**, *40*, 546−551.
(29) Quéré, D. Wetting and Roughness. *Annu. Rev. Mater. Res.* **2008**, *38* (1), 71−99.
(30) Bormashenko, E. General Equation Describing Wetting of Rough Surfaces. *J. Colloid Interface Sci.* **2011**, *360*, 317−319.
(31) Fathi, S. J.; Austad, T.; Strand, S. Water-Based Enhanced Oil Recovery (EOR) by "Smart Water": Optimal Ionic Composition for EOR in Carbonates. *Energy Fuels* **2011**, *25*, 5173−5179.
(32) Ayirala, S. C.; Yousef, A. A. A State-of-the-Art Review To Develop Injection-Water-Chemistry Requirement Guidelines for IOR/EOR Projects. *SPE Production & Operations* **2015**, *30* (1), 26−42.
(33) Chen, S.-Y.; Kaufman, Y.; Kristiansen, K.; Dobbs, H. A.; Cadirov, N. A.; Seo, D.; Schrader, A. M.; Andresen Eguiluz, R. C.; Alotaibi, M. B.; Ayirala, S. C.; Boles, J. R.; Yousef, A. A.; Israelachvili, J. N. *New Atomic to Molecular Scale Insights Into SmartWater Flooding Mechanisms in Carbonates*. Paper SPE 190281 presented at the SPE Improved Oil Recovery Conference held in Tulsa, Oklahoma, USA, 14−18 April, 2018.
(34) Muggeridge, A.; Cockin, A.; Webb, K.; Frampton, H.; Collins, I.; Moulds, T.; Salino, P.; Recovery Rates, Enhanced Oil Recovery and Technological Limits. *Philos. Trans. R. Soc., A* **2014**, *372*, DOI: 10.1098/rsta.2012.0320.
(35) Israelachvili, J. N.; Min, Y.; Akbulut, M.; Alig, A.; Carver, G.; Greene, W.; Kristiansen, K.; Meyer, E.; Pesika, N.; Rosenberg, K.; Zeng, H. Recent Advances in the Surface Forces Apparatus (SFA) Technique. *Rep. Prog. Phys.* **2010**, *73*, 036601.
(36) Kristiansen, K.; Valtiner, M.; Greene, G. W.; Boles, J. R.; Israelachvili, J. N. Pressure Solution − the Importance of the Electrochemical Surface Potentials. *Geochim. Cosmochim. Acta* **2011**, *75*, 6882−6892.
(37) Chen, S.-Y.; Kaufman, Y.; Schrader, A. M.; Seo, D.; Lee, D. W.; Page, S. H.; Koenig, P. H.; Isaacs, S.; Gizaw, Y.; Israelachvili, J. N. Contact Angle and Adhesion Dynamics and Hysteresis on Molecularly Smooth Chemically Homogeneous Surfaces. *Langmuir* **2017**, *33* (38), 10041−10050.
(38) Bouchelaghem, F. A numerical and analytical study on calcite dissolution and gypsum precipitation. *Appl. Math. Model.* **2010**, *34*, 467−480.
(39) Yousef, A. A.; Al-Saleh, S. H.; Al-Kaabi, A.; Al-Jawfi, M. S. Laboratory Investigation of the Impact of Injection-Water Salinity and Ionic Content on Oil Recovery from Carbonate Reservoirs. *SPE Reservoir Eval. Eng.* **2011**, *14* (05), 578−593.

DOI: 10.1021/acs.langmuir.8b02711
Langmuir 2019, 35, 41−50